# Resonant phenomena of hyper-Raman-scattering of optic phonons in a $TiO_2$ crystal

Kenji Watanabe,* Kuon Inoue, and Fujio Minami
*Research Institute for Electronic Science, Hokkaido University, Kita-ku, Sapporo 060, Japan*
(Received 10 September 1991)

We report two-photon-resonant phenomena of hyper-Raman-scattering by optic phonons in $TiO_2$. It is found that the scattering efficiency of the allowed mode in the 90°-scattering geometry increases remarkably as twice the incident photon energy, $2\hbar\omega_i$, approaches the direct forbidden energy gap from below. In addition, the configuration-forbidden LO mode in the backward-scattering geometry is found to show a sharp two-photon-resonant behavior at the band edge. The prominent polarization dependence of the phenomena is observed, reflecting the anisotropic nature of $TiO_2$. Further, the absolute value of the scattering efficiency is estimated as a function of $2\hbar\omega_i$. It is shown that these results can be interpreted quantitatively with a model on the basis of the electronic band structure. In the course of the analysis, we have estimated the second-lowest-direct-gap energy as 3.10 eV. Finally, we emphasize that the resonant hyper-Raman spectroscopy would be useful as a method for studying the band structure in solids.

## I. INTRODUCTION

Hyper-Raman-scattering spectroscopy in crystals is an important method for gaining information about Raman-inactive phonon modes. Many works have been reported in this respect.[1] For example, it is established to be one of the most useful methods for studying the structural phase transition of solids in the case where the relevant soft optic phonon is Raman forbidden.[2–5] However, little attention has been paid, so far, to resonant effects of hyper-Raman-scattering.

Hyper-Raman-scattering is an incoherent nonlinear scattering such that two incident photons $\hbar\omega_i+\hbar\omega_i$ in energy are annihilated with one new photon (scattered) $\hbar\omega_s$ and one phonon $\hbar\omega_q$, both created behind. Consequently, the hyper-Raman-scattering strength, which is dependent on the intensity of incident light, may be characterized by a ratio $S_{\rm HR}/I_L$ [cm (MW sr)$^{-1}$] of the scattering efficiency $S_{\rm HR}$ (differential scattering cross section per unit volume) against the intensity or power flux $I_L$, which is the normalized hyper-Raman efficiency proposed by Vogt and Rossbroich.[6] In the one-phonon process, it is given (cgs units) by

$$\frac{S_{\rm HR}}{I_L}=\frac{2\pi\omega_s^3\omega_i}{\eta_i c^5}\frac{\hbar}{2MN\omega_q}\frac{\eta_s}{\eta_i}[N(\omega_q)+1]|d_{\rm HR}|^2 . \quad (1)$$

Here, $N$ is the number of unit cells in the unit volume, $M$ the reduced mass of the atoms contributing to the optic mode, $N(\omega_q)$ the Bose-Einstein factor of the phonon, $c$ the speed of light and $\omega_q$ the phonon frequency, $\eta$ and $\omega$ are the refractive index and the frequency of light, the indices $i$ and $s$ refer, throughout the present paper, to incident and scattered lights, respectively, and $d_{\rm HR}$ is the hyper-Raman tensor for the relevant phonon $q$. In the framework of time-dependent perturbation formalism, $d_{\rm HR}$ can be written to the dipole approximation as,[7]

$$|d_{\rm HR}|^2=\left|\frac{e^3}{am^3\omega_i^2\omega_s V}\left[\sum_{l,m,n}\frac{P_{gn}D_{nm}P_{ml}P_{lg}}{(E_n-\hbar\omega_s)(E_m-2\hbar\omega_i)(E_l-\hbar\omega_i)}+\cdots\right]\right|^2 , \quad (2)$$

where $m$ and $e$ are the electron mass and charge, $V$ the volume of crystal, and $a$ the lattice constant. The indices $l$, $m$, and $n$ refer to the intermediate states of electronic excitation with their respective energies $E_\alpha$ ($\alpha=l,m,n$), and $P_{lm}$ and $D_{lm}$ are the respective matrix elements of the momentum operator and the electron-phonon interaction. In the TO phonon scattering, $D_{lm}$ represents the deformation potential as defined by Bir and Pikus,[8] while in the LO phonon scattering, the Fröhlich interaction is added to $D_{lm}$. The major dependence of the hyper-Raman tensor on the incident photon energy arises from the resonant denominators in Eq. (2). A resonant enhancement should occur when either one of the relevant photon energies, $\hbar\omega_i$, $\hbar\omega_s$, and $2\hbar\omega_i$, or two of them simultaneously, become close to the energies of some specific intermediate states $l$, $m$, and $n$, such as those of the fundamental and higher-energy gaps of the crystal. In the two-photon resonance case that we are concerned with, a term $\{(E_n-\hbar\omega_s)(E_m-2\hbar\omega_i)\}^{-1}$ in Eq. (2) should contribute primarily to the resonant enhancement. Recently, we reported such resonant phenomena of hyper-Raman-scattering in $SrTiO_3$ and

 

$TiO_2$.[9–11] The scattering efficiency of the allowed modes was found to increase remarkably, as $2\hbar\omega_i$ approached the direct energy gap $E_g$ from below. Further, the LO mode forbidden in the backward-scattering geometry in the usual selection rules was also found to show a two-photon-resonant behavior at the band edge. As for $TiO_2$, we made a tentative interpretation of the results.

The purpose of the present paper concerning $TiO_2$ is to report a full interpretation as well as detailed features of the resonant effects. We also report additional information about the electronic structure of $TiO_2$ crystal in the vicinity of the band edge, which we have clarified in the course of analyses of the resonant effect. We have also made a two-photon absorption measurement.

First, for later use, we describe briefly information about the electronic structure reported thus far, which is still controversial to some extent, although a number of studies[12–15] have been done. As far as the lowest gap is concerned, it has been characterized from both the experimental and theoretical points of view. Pascual, Camassel, and Mathieu[12] have carefully investigated the absorption edge of $TiO_2$ by one-photon absorption measurements. Their results are as follows. The lowest direct transition is strictly forbidden in polarization parallel to the $z$ axis ($c$ axis) but weakly allowed through higher-order approximation, in polarization perpendicular to the $z$ axis. They have also found that the direct gap is located at 3.034 eV in energy at 30 K and is composed of a series of excitons, with a binding energy of $1s$ exciton of 4 meV. Direct creation of $1s$ and $p_{xy}$-type excitons is allowed in the one-photon absorption only through the second-order approximation. The creation of $p_z$-type exciton is totally forbidden. By investigating the effect of uniaxial compression up to 24 kbar on the direct and indirect absorption edges, they have confirmed the above assignment concerning the direct forbidden edge.[13] Theoretically, Jourdan, Gout, and Albert[17] have calculated the band structure of $TiO_2$, which is a more sophisticated version of the one given by Daude, Gout, and Jouanin.[16] The results agree qualitatively well with the experimental ones described above. The energy band scheme they have derived is shown in Fig. 1 for later use, where the one-photon transition from the maximum of valence band $\Gamma_{7+}^{v}$ to the lowest conduction band of $\Gamma_{6+}^{c}$ is forbidden to the electric-dipole approximation for both polarizations $\mathbf{e}_i \| \hat{\mathbf{z}}$ and $\mathbf{e}_i \perp \hat{\mathbf{z}}$. Here the superscripts $c$ and $v$ denote conduction and valence bands, respectively. This transition is allowed through two-photon absorption with one of the two-photon polarizations $\mathbf{e}_i, \mathbf{e}_j$ perpendicular to the $z$ axis, i.e., $xx$, $yy$, $xy$, $xz$, and $yz$. As for $\mathbf{e}_i \| \hat{\mathbf{z}}$, the one-photon absorption edge is governed by the indirect transition.[12,13] The second-lowest direct gap, which is "lowest" for $\mathbf{e}_i \| \hat{\mathbf{z}}$ is left unclear, although it is likely[17] to be the one corresponding to a transition from spin-orbit split degenerate valence bands $\Gamma_{6+}^{v}$ or $\Gamma_{7+}^{v}$ to the $\Gamma_{6+}^{c}$ conduction band. According to the calculation,[17] this one is also one-photon absorption forbidden, but two-photon allowed for both polarizations; the transition from $\Gamma_{6+}^{v}$ to $\Gamma_{6+}^{c}$ is allowed only for the polarizations of $zz$, and the transition from $\Gamma_{7+}^{v}$ to $\Gamma_{6+}^{c}$ is allowed for $xx$, $yy$, $xy$, $xz$, and $yz$.

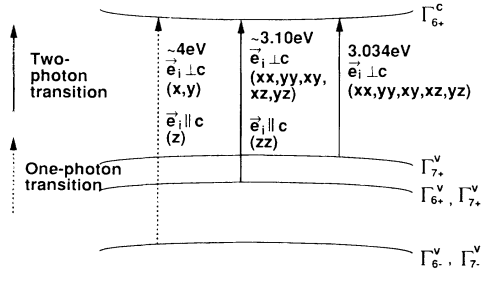


FIG. 1. A schematic band structure of $TiO_2$ together with the optical selection rules, where $c$ and $v$ denote the conduction and valence bands, respectively.

## II. EXPERIMENTAL

Figure 2 shows the experimental setup. All measurements were performed by an ordinary one-beam exciting technique using a home-made dye laser pumped by a Cu-vapor laser (Metalaser model HR1032). A wavelength-tunable range of a dye of styryl-9 was from 843 to 780 nm (1.47 to 1.59 eV) in the present system, $2\hbar\omega_i$ covering the lowest-band-gap energy, i.e., $E_g = 3.034$ eV (408.5 nm in wavelength). The dye laser had the output characteristics of typically 3 kW in peak power with 15-nsec pulse width and 6-kHz pulse repetition rate. The beam from the dye laser was focused onto a sample by an objective with $f = 3$ cm. We checked the relation that the signal was proportional to the square of the laser power.

The samples cut from a colorless single boule of $TiO_2$ single crystal were prepared in the parallelepiped form of $4 \times 4 \times 6$ mm$^3$ in dimension. All surfaces were carefully polished to be optically flat. The sample was set in a helium-gas-flow-type cryostat and was cooled to 30 K. The scattered radiation from the sample was collected by a lens, dispersed with a monochromator (Ritsu MC-25NP), and detected with an optical multichannel detec-

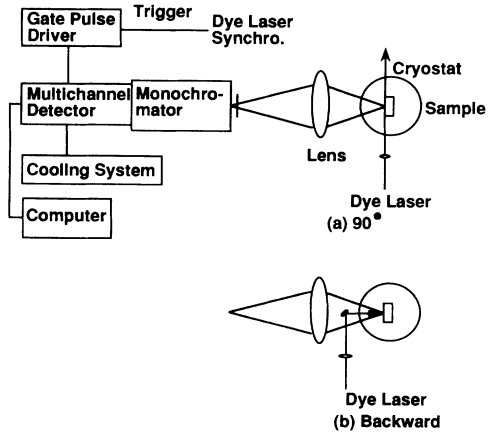


FIG. 2. Experimental arrangement for resonant hyper-Raman-scattering measurement, where (a) and (b) are schematics of 90°- and backward-scattering configurations, respectively.

tor (Tracor Northern TN-6133). Cooling the detector below −40 °C enabled one to accumulate the signal for more than 30 min since thermal noises were drastically reduced, thereby resulting in great improvement of sensitivity with a simultaneous use of gate operation synchronized with the laser pulses. The dye laser power was monitored by a thermopile detector.

To extend the frequency region, and to compare the relative magnitude of signals between in-resonance and in far off-resonance, we also employed a $Q$-switched Nd-doped yttrium aluminum garnet (YAG) laser ($\hbar\omega_i = 1.16$ eV) as another excitation source. A normalization procedure is obviously needed to directly compare the scattering efficiency between two kinds of excitation, since the characteristics of both lasers are quite different, i.e., concerning the laser mode, power, and repetition rate. For this purpose, we utilized a KI crystal as a reference, since frequency dispersion of the efficiency for KI crystal whose band-gap energy is about 6 eV, might be neglected. In addition, the absolute scale of the efficiency was also obtained by comparing the present measurement in the configuration of $x(zz,z)\bar{x}$ with the data of TO scattering in KI in the literature,[18] $S_{\rm HR}/I_L = 10^{-17}$ cm (MW sr)$^{-1}$ for Nd-YAG laser excitation.

## III. RESULTS

### A. Allowed scattering

Taking the anisotropic nature of $TiO_2$ into consideration, the measurements were made in two configurations such as $x'(zz,o)z$ ($\mathbf{e}_i \| \hat{\mathbf{z}}$) and $x'(y'y',o)z$ ($\mathbf{e}_i \perp \hat{\mathbf{z}}$), where the first two notations and the last one in the parentheses refer to the polarization directions of incident and scattered lights, and $x'$, $y'$, and $o$ denote $\langle 1,1,0\rangle$, $\langle 1,\bar{1},0\rangle$, and unpolarized directions, respectively. In these configurations the TO and LO phonons of $E_u$ symmetry and $E_u$-$A_{2u}$ mixed symmetry (oblique modes) are allowed. The examples of the hyper-Raman spectrum observed for dye-laser excitation with $2\hbar\omega_i = 2.94$–$3.12$ eV are shown in Fig. 3. The abscissa in Fig. 3 is plotted as a frequency shift from the value $2\hbar\omega_i$ in cm$^{-1}$ with the Stokes shift being positive. Mode assignment of the observed spectral lines were made on the basis of a detailed polarization measurement[19] at room temperature. Two $E_u$(TO)+$E_u$(LO) modes, not fully resolved in the present resolution power, and one oblique $E_u$-$A_{2u}$ mode (TO,LO) were observed as labeled in Fig. 3. The frequencies of the observed lines shift a few cm$^{-1}$ from those values at room temperature. It is found that as the value of $2\hbar\omega_i$ approaches from below to the fundamental absorption edge, the hyper-Raman signal becomes appreciably intense. Further increase of the excitation energy such that $2\hbar\omega_i$ is in the absorption range results in diminishing the magnitude of the raw signal. Examples of those spectra are also shown in Fig. 3 for the values of $2\hbar\omega_j$ beyond 3.03 eV. In addition to these signals, weak emissions labeled with dashed bars in Fig. 3 were also observed when $2\hbar\omega_i$ exceeded the respective threshold energies, 3.10 and 3.03 eV for $\mathbf{e}_i \| c$ and $\mathbf{e}_i \perp c$. The detail will be described later.

Variation of the efficiency $S_{\rm HR}/I_L$ as a function of $2\hbar\omega_i$ was estimated over a region including the lowest band edge. In estimating the efficiency, we made some corrections to the magnitude of the raw signal; those include the ones due to the wavelength dependences of optical tool's transmission and detector's sensitivity, dye-laser power, and reabsorption of scattered light. Figure 4 shows the result thus obtained for the $E_u$-$A_{2u}$ oblique LO mode at 810 cm$^{-1}$ in both polarization cases. Owing

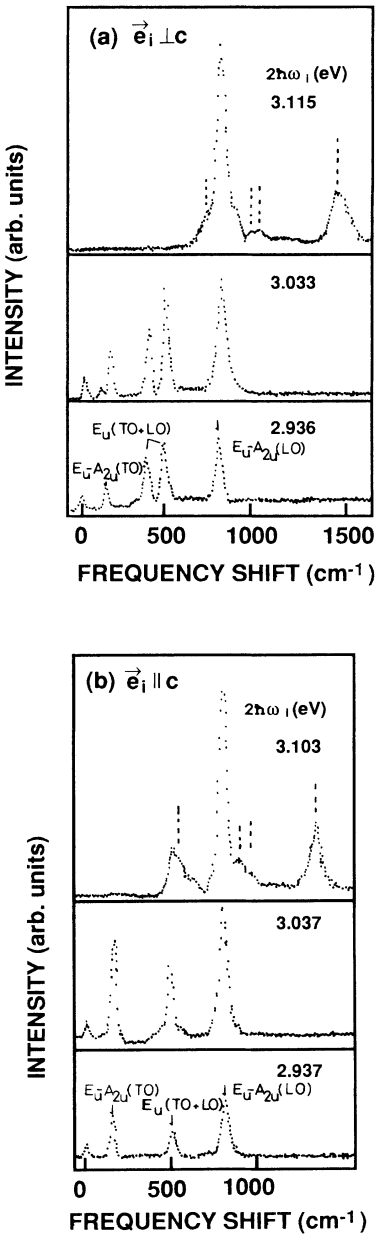


FIG. 3. Examples of the hyper-Raman spectrum in the 90°-scattering geometry excited by a dye laser in $TiO_2$ at 30 K for the polarizations, (a) $\mathbf{e}_i \perp c$ and (b) $\mathbf{e}_i \| c$. Twice the excitation photon energy is in the range of 2.93–3.12 eV. The dotted bars denote the two-photon-excited emissions. The respective spectral widths of the emissions and the scattered components are typically 100 cm$^{-1}$ and 50 cm$^{-1}$, which are well larger than the resolution power of our system (30 cm$^{-1}$).

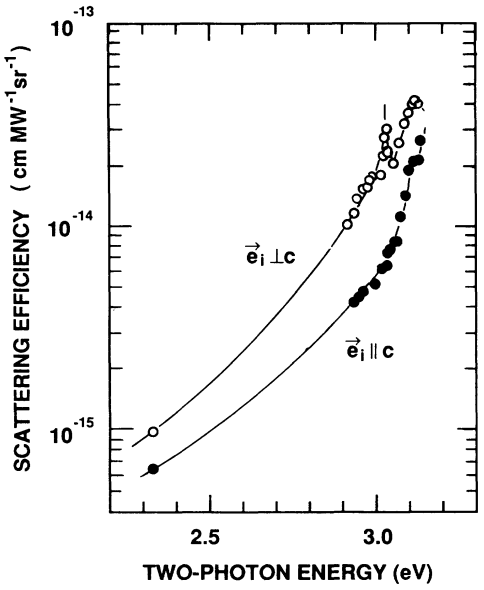


FIG. 4. A plot of the scattering efficiency as a function of $2\hbar\omega_i$ for the allowed LO-oblique phonon with the energy of 810 cm$^{-1}$ for respective polarizations. The bar indicates the position of the lowest direct-forbidden band gap. The lines are a guide to the eye.

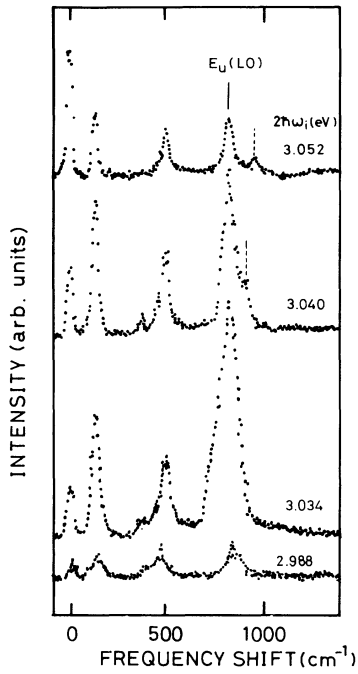


FIG. 5. Examples of the hyper-Raman spectrum in the backward-scattering geometry excited by a dye laser in $TiO_2$, where the forbidden $E_u$(LO) mode (labeled) is observed at 816 cm$^{-1}$, other than the allowed scattering signal, i.e., $A_{2u}$(TO) and three $E_u$(TO) modes. Weak emission lines indicated by the dotted lines are also observed. The spectral width of the LO scattering component is not recognized to be clearly narrower than that of the emission ($\sim 100$ cm$^{-1}$).

to the highest frequency shift, the measurement on this mode could be carried out in the widest frequency region with respect to $2\hbar\omega_i$, i.e., a region beyond the band gap where the signal gradually suffered indirect absorption. Correction due to the absorption is needed only for a few data points above 3.1 eV in Fig. 4. This is because the correction factor arising from this absorption may be expressed as $1/\exp(-\alpha d)$, in which $\alpha$ and $d$ represent the absorption coefficient at scattered photon frequency and the path length, respectively. It is noted that the signal in the higher-energy region beyond 3.13 eV in Fig. 4 could not be observed in the present detection system, because of the strong indirect absorption.

It is clearly seen in Fig. 4 that a remarkable enhancement of the efficiency occurs for both polarization cases ($\mathbf{e}_i \| c, \mathbf{e}_i \perp c$), as the value $2\hbar\omega_i$ approaches the direct gap $E_g$, and that the efficiency still increases beyond it aside from a small peak at 3.03 eV for the case $\mathbf{e}_i \perp c$. The peak, though being small, may correspond to the $S=1$ exciton excitation as described later. It is noted that its existence was experimentally reproducible enough. It is also noted that the trend of the variation, $S_{\rm HR}/I_L$ vs $2\hbar\omega_i$ for the other modes is basically similar to the result shown in Fig. 4, aside from the absolute efficiency.

### B. Forbidden scattering

Next, we describe the result obtained in the backward-scattering geometry of $y(xx, x+z)\bar{y}$, where all phonons other than three $E_u$(TO) and one $A_{2u}$(TO) modes are forbidden in the usual selection rules. However, the forbidden mode could be actually observed like the forbidden resonant Raman-scattering case. Examples of the spectrum are shown in Fig. 5. The spectrum of the forbidden $E_u$(LO) mode at 816 cm$^{-1}$ is seen to be as intense as the TO mode, which is inherently allowed in the present geometry. As the value of $2\hbar\omega_i$ is closer to $E_g = 3.034$ eV, the forbidden signal becomes appreciably intense. Notice that weak emissions were also observed in this configuration for $2\hbar\omega_i$ exceeding $E_g$. The normalized efficiency $S_{\rm HR}/I_L$ of the forbidden mode was estimated as a function of $2\hbar\omega_i$. The result presented in Fig. 6 indi-

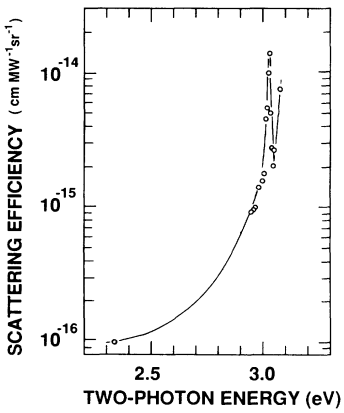


FIG. 6. The dependence of the normalized scattering efficiency on incident photon energy for the forbidden mode in $TiO_2$. The line is a guide to the eye.

cates that a sharp resonance manifests itself around 3.03 eV corresponding to the excitation energy of the $S=1$ exciton.

### C. Two-photon excited emission

As already mentioned, weak emission lines were observed in addition to the hyper-Raman signals when $2\hbar\omega_i$ exceeded the respective threshold energies for $\mathbf{e}_i \| c$ and $\mathbf{e}_i \perp c$ (Fig. 3). The absolute energies labeled with bars in Fig. 3 are 3.034, 2.987, 2.975, and 2.933 eV from the left, respectively. Their absolute energies did not shift when the excitation photon energy was varied. Therefore, they should be not scattered signals but emissions. It is reasonable that these emission lines are assigned as those due to phonon-assisted dipole transitions from the lowest conduction to the highest valence band. The energy of the line at 3.034 eV corresponds just to the energy of the one-photon-forbidden lowest direct gap. Therefore, we have assigned it as an emission due to a higher-order process. The other three lines are found to shift by 380, 475, and 816 $cm^{-1}$ to the lower-energy side from the gap energy, respectively. Those values correspond to $E_u$(LO) phonon energies at the Brillouin-zone center. Thus, we can assign them as $E_u$(LO)-phonon-assisted emissions from the lowest conduction band to the topmost valence band. The intensity variation of the emission line with the shift of 816 $cm^{-1}$ with $2\hbar\omega_i$ is shown in Fig. 7, where the respective thresholds are denoted by bars. It is reasonable that the threshold energy of 3.03 eV for $\mathbf{e}_i \perp c$ just corresponds to the lowest-band-gap energy. The threshold energy of 3.10 eV for $\mathbf{e}_j \| c$, on the other hand, should correspond to the second-lowest-direct-gap energy, as will be argued later.

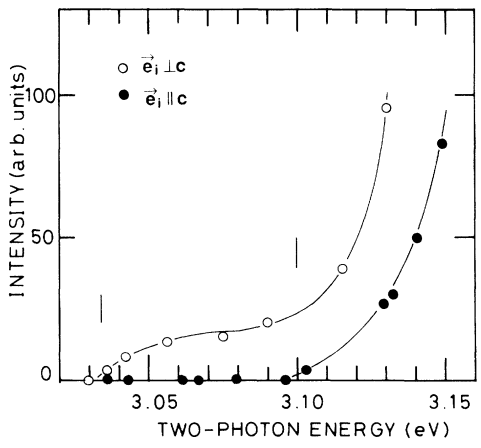


FIG. 7. Two-photon excitation spectra of LO-phonon-assisted emission in the 90°-scattering geometry for the respective polarizations in $TiO_2$ where the bars indicate the direct band edges. The lines are a guide to the eye. The intensity of the emission for the polarization $\mathbf{e}_i \perp c$ decreases monotonously with the decrease of $2\hbar\omega_i$ until 3.034 eV, around where the emission cannot be resolved.

## IV. ANALYSIS OF EXPERIMENTAL RESULTS

We show below that the experimental results on the allowed and forbidden scatterings may be interpreted as caused by different mechanisms, but in a consistent way from the band-structural point of view. Accordingly, we treat them separately.

### A. Allowed scattering

The major resonant behavior of the allowed mode might be well interpreted in terms of a three-band model as follows. The electron-radiation ($H_{ER}$) and electron-lattice ($H_{EL}$) interactions involved in the allowed hyper-Raman-scattering process should be of interband nature in the case of a centrosymmetric solid such as $TiO_2$. This is because the states should have their definite parities at the high-symmetry points of the Brillouin zone, indicating that the matrix elements concerning the intraband transition should vanish. In Fig. 8 we illustrate a schematic diagram of a series of virtual electronic transitions which should play a dominant role in the present process. There, the numbers 1, 2, 3, and 4 designate a successive order of virtual electronic transitions through either the $H_{ER}$ (not described in Fig. 8) or $H_{EL}$. As already described in Sec. I, a dominant term of the hyper-Raman tensor $|d_{HR}|$ may come from the first term of Eq. (2) containing a resonant denominator with respect to $2\hbar\omega_i$ or $\hbar\omega_s$. The electronic system initially in the

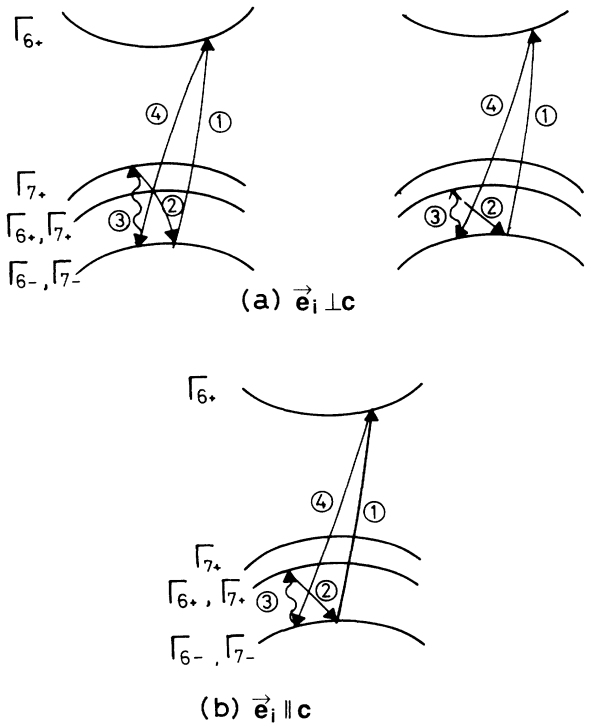


FIG. 8. Schematic diagram showing the mechanism of resonance for the allowed scattering in the framework of time-dependent perturbation formalism. The numbers 1, 2, 3, and 4 indicate a time order of successive electronic transitions.

ground state $|g\rangle$ is excited through dipole interband excitation (transition 1) to an intermediate continuum state $|l\rangle$ composed of electron-hole pair, followed by a transition 2 to another pair state $|m\rangle$. Then, through third intermediate state $|n\rangle$ reached by the electron-lattice interaction, the system comes back to the ground state through a dipole transition 4. Therefore, in the case of $\mathbf{e}_i \perp c$, the two-photon-allowed intermediate state $|m\rangle$ may be either the one corresponding to the lowest direct gap at 3.034 eV ($\Gamma^v_{7+}$-$\Gamma^c_{6+}$) or the other corresponding to the second-lowest direct gap at 3.10 eV ($\Gamma^v_{7+}$-$\Gamma^c_{6+}$). We assume the states $|l\rangle$ and $|n\rangle$ as the same for simplicity. Considering the band structure together with one-photon absorption data,[14] the most likely intermediate states for $|l\rangle$ and $|n\rangle$ may be those of degenerated $\Gamma^v_{6-}$ and $\Gamma^v_{7-}$ valence bands, which lie about 1.0 eV below the highest $\Gamma^v_{7+}$ band. The intermediate state $|m\rangle$ in the case of $\mathbf{e}_i \| c$, on the other hand, may be the one corresponding to the second-lowest forbidden gap ($\Gamma^v_{6+}$-$\Gamma^c_{6+}$), assuming $|l\rangle$ and $|n\rangle$ to be the same, as before.

An attempt of theoretical fitting was made with the above models in the following way. We first estimated the absolute squared hyper-Raman tensor $|d_{\mathrm{HR}}|^2$ from the experimental values of the efficiency in Fig. 4 in terms of Eq. (1). The result is shown with open circles in Fig. 9. Then, assuming a set of parabolic valence and conduction bands, we calculated the respective fitting curves:

$$|d_{\mathrm{HR}}|^2 = \left| \frac{e^3}{am^3\omega_i^2\omega_s V}(BI + B'I' + C) \right|^2 \quad (\mathbf{e}_i \perp c) \tag{3}$$

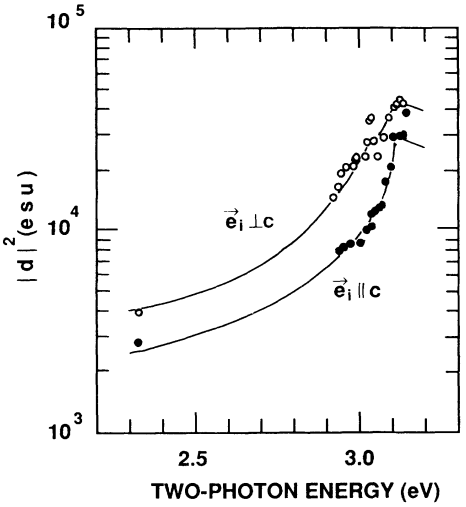


FIG. 9. Frequency dispersion of the squared hyper-Raman tensor of the allowed scattering and theoretical fitting curves (solid lines).

and

$$|d_{\mathrm{HR}}|^2 = \left| \frac{e^3}{am^3\omega_i^2\omega_s V}(B'I' + C') \right|^2 \quad (\mathbf{e}_i \| c)\,, \tag{4}$$

where $I$ and $I'$ denote

$$I = \frac{V}{4\pi}\int \frac{d^3K}{(E_g^u + \hbar^2K^2/2\mu - \hbar\omega_s)(E_g^g + \hbar^2K^2/2\mu - 2\hbar\omega_i)(E_g^u + \hbar^2K^2/2\mu - \hbar\omega_i)}\,, \tag{5}$$

$$I' = \frac{V}{4\pi}\int \frac{d^3K}{(E_g^u + \hbar^2K^2/2\mu - \hbar\omega_s)(E_g^{2g} + \hbar^2K^2/2\mu - 2\hbar\omega_i)(E_g^u + \hbar^2K^2/2\mu - \hbar\omega_i)}\,. \tag{6}$$

Here $K$ is a wave vector of electron (or hole) state, $\mu$ the reduced effective mass, $a$ the average lattice constant, $E_g^g$ and $E_g^u$ the lowest direct-forbidden and the lowest one-photon-allowed gaps, respectively, $E_g^{2g}$ the second-lowest direct forbidden gap. The superscripts $u$ and $g$ denote their parities, "ungerade" (odd) and "gerade" (even), respectively. $C$ and $C'$ denote nonresonant terms which are assumed to be constant almost independent of frequency. The constants $B$ and $B'$ are given by

$$B = P_{gu}D_{ug}P_{gu}P_{ug} \tag{7}$$

and

$$B' = P_{gu}D_{u2g}P_{2gu}P_{ug}\,. \tag{8}$$

Here we assumed that the matrix elements concerning $P$ and $D$ are independent of $K$. Using Eqs. (3) and (4), a

TABLE I. Numerical values of the parameters used for the theoretical fit in Fig. 9.

| Parameter | Value | Ref. |
|---|---|---|
| $E_g^u$ | 4.0 eV | 14 |
| $E_g^g$ | 3.034 eV | 12,13 |
| $E_g^{2g}$ | 3.10 eV | |
| $\mu$ | $8.4m_0$ | 12 |
| $a$ | 4.0 A | a |
| $M$ | $20M_p$ | a |
| $P_{mn}$ | $2.6\times10^{-20}$ esu | b |
| $D(\Gamma_{6+,7+}$-$\Gamma_{6+})$ | 4.4 eV | Fit |
| $D'(\Gamma_{7+}$-$\Gamma_{6+})$ | 2.2 eV | Fit |
| $C$ $(\mathbf{e}_i \perp c)$ | 63 esu | Fit |
| $C'$ $(\mathbf{e}_i \| c)$ | 53 esu | Fit |

[a]The average value was used. Here, $M_p$ is a proton mass.
[b]This value was calculated from the expression $P \sim \hbar/a$.

computer fit was made. In doing so, $B$, $B'$, and $C$ for $\mathbf{e}_i \perp c$, $B$ and $C$ for $\mathbf{e}_i \| c$ were regarded as adjustable parameters. The solid lines in Fig. 9 show the best-fit results with values of adjustable parameters listed in Table I.

### B. Forbidden scattering

We are especially concerned with the mechanism of a sharp resonance at 3.03 eV, aside from the whole curve of $S_{\mathrm{HR}}/I_L$ vs $2\hbar\omega_i$ in Fig. 6. We therefore argue the origin first.

It may be suggestive to understand the mechanism of the forbidden resonant Raman scattering, which has been extensively studied. It is clarified that the $q$-dependent Fröhlich mechanism gives rise to the forbidden scattering in polar semiconductors. According to the recent calculations by Trallero-Giner, Cantarero, and Cardona,[20,21] a discrete-discrete exciton transition through the $q$-dependent Fröhlich interaction plays a key role in the forbidden process. Having the above in mind, the present resonant behavior at 3.03 eV can be interpreted in terms of a simple mechanism where $1s$ and $2p$ excitons are predominantly involved as the second and third intermediate states, and the $q$-dependent intraband Fröhlich interaction is responsible for the transition 3 between them. Note that a second kind of exciton is known to exist in $TiO_2$ as already described. The whole process is illustrated in Fig. 10. There, a higher-order transition is assumed to cause the transition 4 from the $2p$ exciton to the ground state. In this case, the hyper-Raman tensor may be written in the form,

$$|d_{\mathrm{HR}}| = |\mathbf{e}_i \cdot d_{\mathrm{HR}}^{i,j,k,l,m} : \mathbf{e}_j \mathbf{e}_k \mathbf{k}_i^l \mathbf{q}_m| \ , \tag{9}$$

where $k_i$ is the Cartesian component of the wave vector

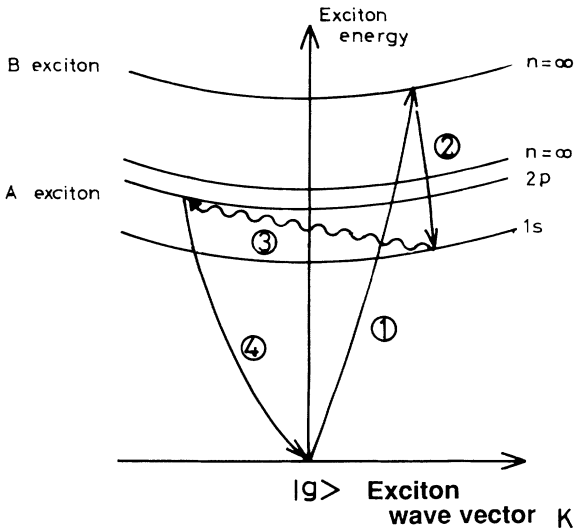


FIG. 10. Schematic diagram showing the mechanism of resonance for the forbidden scattering in the time-dependent perturbation formalism. $A$ excitons and $B$ excitons are constituted from a hole and an electron belonging to $\Gamma_{7+}^{v}$-$\Gamma_{6+}^{c}$ ($E_g = 3.034$ eV), $\Gamma_{6-,7-}^{v}$-$\Gamma_{6+}^{c}$ ($E_g \sim 4.0$ eV), respectively.

of the scattered photon. Using a relationship between the hyper-Raman tensor and the crystal-space-group Clebsch-Gordan coefficients,[22,23] non-vanishing elements of the tensor can be deduced. The result is shown in Table II. In the configuration of $y(xx,x+z)\bar{y}$, the tensor has actually nonzero components such as $d_{xxx,zxx}$. More concretely, it can be shown that $d_{\mathrm{HR}}$ is expressed as

$$|d_{\mathrm{HR}}|^2 = \left| \frac{e^3}{m^3} \left[ \frac{2MN\omega_q}{\hbar} \right]^{1/2} \frac{C_F^* \nabla_K P_{2p} P_{1s} P_c}{E_g \omega_i^2 \omega_s q} \left[ \frac{\nabla_r \Psi_{2p}(0)\{I_{c,v}(-\mathbf{q}_h) - I_{c,v}(\mathbf{q}_e)\}\Psi_{1s}(0)}{(E_{2p} - \hbar\omega_s + i\Gamma_{2p})(E_{1s} - 2\hbar\omega_i + i\Gamma_{2s})} \right] \right|^2 , \tag{10}$$

where $E_{1s}$ and $E_{2p}$ denote $1s$ and $2p$ exciton excitation energies, $\Gamma_{1s}$ and $\Gamma_{2p}$ the lifetime broadenings of the respective states, $\Psi_{2p\,\mathrm{or}\,1s}(r)$ the wave function of the internal exciton; the term, $\nabla_k P_{2p}$ indicates that the transition 4 in Fig. 10 represents higher-order dipole transition, and $P_{1s,c}$ the matrix element of the respective dipole moment. $C_F$ and $I_{c,v}(\mathbf{q}_\alpha)$ ($\alpha = e,h$: electron and hole) are equal, respectively, to

$$C_F^* = -i \left[ 2\pi\hbar\omega_q e^2 \left[ \frac{1}{\varepsilon_\infty} - \frac{1}{\varepsilon_0} \right] \right]^{1/2} , \tag{11}$$

$$I_{c,v}(\mathbf{q}_\alpha) = \int d^3\mathbf{r} \Psi_c^*(\mathbf{r}) e^{-i\mathbf{q}_\alpha \cdot \mathbf{r}/a_B} \Psi_v(\mathbf{r}) \ , \tag{12}$$

$\varepsilon_0$ and $\varepsilon_\infty$ being the static and optical dielectric constants, $a_B$ the exciton Bohr radius, $m_e$ and $m_h$ the effective mass of the electron and hole. It is noted that Eq. (10) provides a Lorentzian shape for the result in the region of the band edge.

The theoretical curve based on Eq. (10) is shown in Fig. 11 with solid lines. Numerical values of the parameters obtained by a theoretical fitting in Fig. 11 are listed in Table III. A set of parameters used are referred to

TABLE II. Hyper-Raman tensors and nonvanishing elements for the forbidden $E_u$(LO) mode in the backward-scattering configuration, i.e., $y(xx,x+z)\bar{y}$, in $TiO_2$. The hyper-Raman tensors are calculated on the basis of the higher-order scattering process (see Fig. 10).

$TiO_2$ $y(xx,x+z)\bar{y}$, $\mathbf{k}_s \| \langle 0\bar{1}0 \rangle$, $\mathbf{q} \| \langle 010 \rangle$

| Phonon mode | Hyper-Raman tensor | Nonvanishing element |
|---|---|---|
| $E_u$(LO); | $\begin{matrix} e & f_1 & 0 \\ f_1 & e & 0 \\ 0 & 0 & a \end{matrix}$ | $e$ |

TABLE III. Numerical values of the parameters used for the theoretical fit in Fig. 11.

| Parameter | Value | Ref. |
|---|---|---|
| $E_B$ | 4 meV | 12 |
| $E_g$ | 3.034 eV | 12 |
| $\epsilon_\infty$ | 7 | 1 |
| $\epsilon_0$ | 200 | 1 |
| $\nabla P_{nm}$ | $1.0\times10^{-27}$ | a |
| $q$ | $4.8\times10^{7}$ cm$^{-1}$ | b |
| $m_e$ | $18m_0$ | Fit |
| $m_h$ | $14m_0$ | Fit |
| $\Gamma$ | 4 meV | Fit |

[a]The calculated value in terms of $P_{nm}a$.
[b]A value under the requirement of the momentum conservation law.

mainly from Ref. 12. The effective masses $m_e$, $m_h$, and $\Gamma$ were determined as adjustable parameters. The effective masses $m_e$ and $m_h$ correspond to those at the critical points $\Gamma_{6+}$, and $\Gamma_{7+}$, respectively.

## V. DISCUSSION

First of all, it should be noted that all the scattered TO and LO components are not Raman signals excited by defect-induced second-harmonic light (SHG), but unquestionably hyper-Raman signals. This is because the observed SHG intensity was very weak, as should be, in any scattering geometry, including even the forward-scattering geometry, i.e., as weak as those of the scattered signals, and consequently, it is impossible for such a weak SHG to excite Raman signals of the same order of magnitude. Notice that the mutual exclusion selection rules hold between the Raman and hyper-Raman-scatterings in the centrosymmetric crystals like $TiO_2$, indicating that the polar modes in question are normally forbidden in Raman scattering.

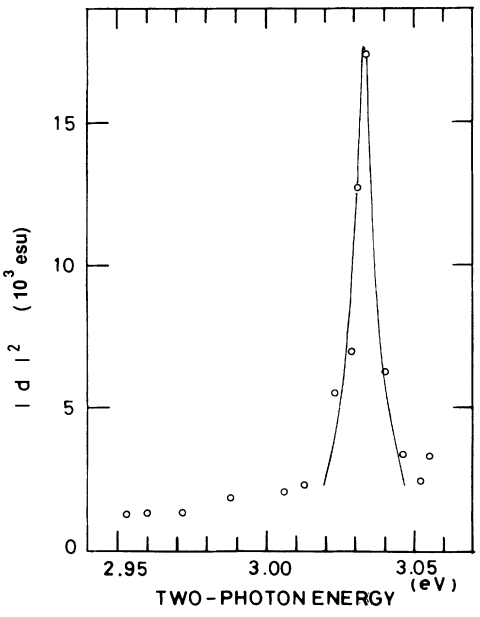


FIG. 11. Frequency dispersion of the squared hyper-Raman tensor of the forbidden mode. A theoretical one (solid line) is compared to the data points concerning the sharp resonant profile around the band edge.

It is also noted that when twice the incident photon energy lies just on the lowest-band-gap energy 3.034 eV, the LO-phonon-assisted emission and the scattered LO component are generally indistinguishable since they appear at the same absolute energy. Even in that case, however, the intensity of the emission component may be sufficiently weaker than that of the scattered component. This postulation may be justified for the following two reasons: (1) In the 90°-scattering geometry, the respective spectral widths of the emission and the scattered signal are 100 cm$^{-1}$ and 50 cm$^{-1}$ in the vicinity of the band gap, as can be seen in Fig. 3(a). The fact that the spectral width of the signal in question stays almost 50 cm$^{-1}$ even in resonance gives evidence in the 90°-scattering case. In the 180°-scattering geometry, on the other hand, the spectral width of the hyper-Raman signal is not recognized to be clearly narrower than that of the emission. However, a plot of the relative emission intensity vs $2\hbar\omega_i$ in the 90°-scattering geometry shows a monotonously decreasing behavior with the decrease of $2\hbar\omega_i$ until 3.034 eV around where the emission can not be resolved (Fig. 7). Accordingly, a reasonable assumption that variation of the relative emission intensity with $2\hbar\omega_i$ in the 180° scattering should be identical to that in the 90° scattering should support the above postulation, i.e., the scattered component causes a prominent anomaly in just resonance. (2) The frequency dependence of LO vs TO scattering intensity ratio for the allowed configuration is found to be constant around 3.034 eV. If the intense LO emission component is superposed on the scattered component, the anomaly at 3.034 eV could be seen for the LO- to TO-intensity ratio of the allowed configuration. This may also support the above statement.

The fitting result of the allowed scattering shown in Fig. 9 is rather satisfactory for the respective polarizations; the major resonant enhancement of the hyper-Raman tensor over a range $2\hbar\omega_i=2.33-3.12$ eV, aside from a small peak at 3.03 eV ($\mathbf{e}_i\perp c$), could be reproduced well. In addition, an order of magnitude of the adjustable parameters (Table I) obtained may be reasonable. The absolute magnitudes of the electron-lattice interactions were estimated as $D=1$ eV and $D'=2$ eV, respectively, from the values of parameters $B$ and $B'$ using Eqs. (7) and (8), where the matrix element $P$ was approximated in terms of the relation $P\sim\hbar/a$ as $\sim2.6\times10^{-20}$ esu. It is noted that in our model $D$ and $D'$ correspond to the magnitudes of interband electron-lattice interaction for $\Gamma^v_{6-}$-$\Gamma^v_{6+}$ and $\Gamma^v_{7-}$-$\Gamma^v_{6+}$, respectively. No works have been reported yet concerning the magnitude in $TiO_2$. As for the deformation potential for the lowest-direct transition $\Gamma^c_{7+}$-$\Gamma^v_{6+}$, only an order of magnitude was estimated as 0.8–2 eV by Mathieu, Pascual, and Camassel.[13] The order agrees fairly well with the present values.

As for a small peak at 3.03 eV, obviously the present

model could not reproduce it, since exciton effects were neglected. It is well known[20,21] that in the resonant Raman process, exciton states, in particular, discrete ones, must be taken into account as intermediate states, since the process including the exciton states should play a decisive role in the vicinity of the band edge. Therefore, similar exciton effects should be taken into account in the present allowed scattering. In the process taking into consideration only the discrete excitons as intermediate states, the frequency dispersion of the hyper-Raman tensor may be approximated by a Lorentzian function such as $(E_g-2\hbar\omega_i+i\Gamma)^{-1}$, indicating that the exciton effects affect substantially the result only in the vicinity of the band edge. Consequently, it may be valid to neglect the exciton effect in the present behavior except the band-edge region. Thus, we are led to the conclusion that the trend of the dispersion behavior, aside from the small peak at 3.03 eV for $\mathbf{e}_i \perp c$, can be well explained quantitatively in terms of a three-band model.

Next, we proceed to discuss the interpretation of the forbidden scattering. The result of the fitting in Fig. 11 with a simple model is again satisfying in the vicinity of the band edge we are concerned with. We can estimate the magnitude of the effective mass as $m_\mu = 8m_0$ using the relation $m_\mu = m_e m_h/(m_e+m_h)$. This value is in good agreement with the one ($m_\mu = 8.4m_0$) in Ref. 12. On the other hand, the present magnitude of 4 meV for $\Gamma$ is somewhat larger than the value reported in Ref. 9 ($\Gamma = 2$ meV). This slight discrepancy might be attributed to a crude approximation of our present model. To obtain a more accurate estimation of the absolute cross section, a summation over all intermediate states at finite wave vector $q$, including continuum states of the exciton, may be required, which presumably leads to a more reasonable value of $\Gamma$.

As for the lower-energy tail below the sharp resonant profile, the origin is at present not clear to us, but by invoking disorders which violate considerably the wave-vector conservation rule, the above anomalous behavior may be explained, as is the case for the forbidden Raman scattering.[24,25] For example, involvement of the quasi-elastic-scattering of electrons by impurities in the process should violate the selection rule.[26,27] If this is the case, the frequency dispersion of the hyper-Raman efficiency far from the band edge should be similar to that of the allowed mode, apart from the absolute magnitude. That a similar frequency dispersion was observed between the allowed and forbidden scatterings in the transparent region seems to support the present argument.

Finally, we discuss the significance of the present phenomenon. First, it will serve as a spectroscopic method for studying band structure. It is noted that the location of the lowest direct band gap in $TiO_2$ has been confirmed by resonant hyper-Raman-scattering. In addition, the second-lowest direct gap has been unraveled to be of the two-photon-transition-allowed nature with the energy of 3.10 eV. With the help of the result of band calculation in Ref. 17, the gap should correspond to the energy between the degenerated $\Gamma_{6+}$ and $\Gamma_{7+}$ valence band, and $\Gamma_{6+}$ conduction band. Second, the present work concerning signal enhancement in the vicinity of the band gap will open the door to more sensitive hyper-Raman measurements in the future. Notice that the hyper-Raman signal is generally very weak so long as the conventional method is employed. For example, the scattering efficiency for the allowed mode in $TiO_2$ with the use of a dye laser becomes about 10–40 times larger as compared to the case of Nd-YAG laser excitation, which has been employed conventionally in almost all experiments to date. Further, resonant hyper-Raman spectroscopy may be useful for gaining information about the electron-phonon interaction. It is noted that the information may be different generally from the one obtained from resonant Raman experiment, since they obey different selection rules. In this sense, the present spectroscopy will be promising as a spectroscopic tool complementary to resonant Raman spectroscopy. Particularly in the ultraviolet region, it will become a very powerful tool as much as the resonant Raman spectroscopy has been. It is emphasized that the incident photon energy of half the optical transition energy is sufficient, indicating that intense wavelength-tunable near-ultraviolet lasers, which are not readily available at present, are not needed, and that sample damage or heating caused by one-photon absorption can be more or less avoided since the sample is transparent to the incident light.

## VI. CONCLUSIONS

Two-photon-resonance phenomena of the hyper-Raman-scattering from optic phonons in $TiO_2$ have been investigated near the direct forbidden energy gap $E_g = 3.034$ eV. As a result, it was found that the scattering efficiency of the allowed mode increases remarkably as $2\hbar\omega_i$ approaches $E_g$ from below, and the configuration-forbidden LO mode in the back-scattering geometry shows a sharp two-photon-resonant behavior at the band edge. It is shown that these results, including the polarization dependence and the absolute value of the scattering efficiency, can be interpreted with a model based on the electronic band structure. Further, the lowest direct gap at 3.034 eV that has been under some controversy has been confirmed, and the location of the second-lowest gap has been estimated as $E_g = 3.10$ eV.

## ACKNOWLEDGMENTS

The authors would like to acknowledge Dr. A. Yamanaka and Dr. S. Asaka for helpful advice in the experiment. This work was supported by a Grant-in-Aid for Scientific Research from the Ministry of Education, Science and Culture, Japan.

*Present address: Research and Development Group, Oki Electric Industry Co., Ltd., 550-5 Higashiasakawa, Hachioji, Tokyo 193, Japan.

[1]V. N. Denisov, B. N. Mavrin, and V. B. Podobedov, Phys. Rep. **151**, 1 (1987).

[2]K. Inoue and N. Asai, J. Phys. (Paris) Colloq. **42**, C6-430 (1981).

[3]H. Vogt and H. Presting, Phys. Rev. B **31**, 6731 (1985).

[4]See, for example, K. Inoue, Jpn. J. Appl. Phys. **24**, Suppl. 24-2, 107 (1985); H. Vogt, *ibid.*, **24**, Suppl. 24-2, 112 (1985).

[5]K. Inoue, A. Hasegawa, K. Watanabe, H. Yamaguchi, H. Uwe, T. Sakudo, Phys. Rev. B **38**, 6352 (1988).

[6]H. Vogt and G. Rossbroich, Phys. Rev. B **24**, 3086 (1981).

[7]S. S. Jha and J. W. F. Woo, Nuovo Cimento **2B**, 167 (1971).

[8]G. E. Pikus and G. L. Bir, Fiz. Tverd. Tela (Leningrad) **1**, 154 (1959) [Sov. Phys. Solid State **1**, 136 (1959)]; G. L. Bir and G. E. Pikus, *ibid.* **2**, 2287 (1960) [**2**, 2039 (1959)].

[9]K. Inoue and K. Watanabe, Phys. Rev. B **39**, 1977 (1989).

[10]K. Watanabe and K. Inoue, J. Phys. Soc. Jpn. **58**, 726 (1989).

[11]K. Watanabe and K. Inoue, Phys. Rev. B **41**, 7957 (1990).

[12]J. Pascual, J. Camassel, and H. Mathieu, Phys. Rev. Lett. **39**, 1490 (1977); Phys. Rev. B **18**, 5606 (1978).

[13]H. Mathieu, J. Pascual, and J. Camassel, Phys. Rev. B **18**, 6920 (1978).

[14]K. Vos and H. J. Krusemyer, J. Phys. C **10**, 3893 (1977); K. Vos, *ibid.* **10**, 3917 (1977).

[15]H. S. Waff and K. Park, Phys. Lett. **32A**, 109 (1970).

[16]N. Daude, C. Gout, and C. Jouanin, Phys. Rev. B **20**, 5292 (1979).

[17]J. L. Jourdan, C. Gout, and J. P. Albert, Solid State Commun. **31**, 1023 (1979).

[18]H. Vogt, Phys. Rev. B **36**, 5001 (1987).

[19]A. Yamanaka and K. Inoue, Rev. Sci. Instrum. **60**, 3253 (1989).

[20]C. Trallero-Giner, A. Cantarero, and M. Cardona, Phys. Rev. B **40**, 4030 (1989).

[21]A. Cantarero, C. Trallero-Giner, and M. Cardona, Phys. Rev. B **39**, 8388 (1989).

[22]J. L. Birman and R. Berenson, Phys. Rev. B **9**, 4512 (1974).

[23]J. L. Birman, Phys. Rev. B **9**, 4518 (1974).

[24]See, for example, A. Pinczuk and E. Burstein, in *Light Scattering in Solids I,* edited by M. Cardona (Springer-Verlag, Berlin, 1983), Chap. 2; R. M. Martin and L. M. Falicov, *ibid.*, Chap. 3.

[25]M. Cardona, in *Light Scattering in Solids II,* edited by M. Cardona and G. Güntherodt (Springer-Verlag, Berlin, 1982), Chap. 2.

[26]A. A. Gogolin and E. I. Rasbha, Solid State Commun. **19**, 1177 (1976).

[27]J. Menendez and M. Cardona, Phys. Rev. B **31**, 3696 (1985).